



**HAL**  
open science

## **A new method for high resolution curvature measurement applied to stress monitoring in thin films**

Sergey Grachev, Quentin Hérault, Jun Wang, Matteo Balestrieri, Hervé Montigaud, Remi Lazzari, Iryna Gozhyk

► **To cite this version:**

Sergey Grachev, Quentin Hérault, Jun Wang, Matteo Balestrieri, Hervé Montigaud, et al.. A new method for high resolution curvature measurement applied to stress monitoring in thin films. *Nanotechnology*, 2022, 33 (18), 10.1088/1361-6528/ac4a2a . hal-03601084

**HAL Id: hal-03601084**

**<https://hal.science/hal-03601084>**

Submitted on 8 Mar 2022

**HAL** is a multi-disciplinary open access archive for the deposit and dissemination of scientific research documents, whether they are published or not. The documents may come from teaching and research institutions in France or abroad, or from public or private research centers.

L'archive ouverte pluridisciplinaire **HAL**, est destinée au dépôt et à la diffusion de documents scientifiques de niveau recherche, publiés ou non, émanant des établissements d'enseignement et de recherche français ou étrangers, des laboratoires publics ou privés.

# A new method for high resolution curvature measurement applied to stress monitoring in thin films

Sergey Grachev<sup>1</sup>, Quentin Hérault<sup>1</sup>, Jun Wang<sup>1</sup>, Matteo Balestrieri<sup>1</sup>, Hervé Montigaud<sup>1</sup>, Rémi Lazzari<sup>2</sup>, Iryna Gozhyk<sup>1</sup>

<sup>1</sup> Surface du Verre et Interfaces, UMR 125 CNRS/Saint-Gobain Recherche, 39 quai Lucien Lefranc, 93303 Aubervilliers, France

<sup>2</sup> CNRS UMR 7588, Sorbonne Université, Institut des NanoSciences de Paris, 4 place Jussieu, 75005 Paris, France

E-mail: sergey.grachev@saint-gobain.com

E-mail: quentin.herault@saint-gobain.com

E-mail: jun.wang@epfl.ch

E-mail: matteo.balestrieri@saint-gobain.com

E-mail: herve.montigaud@saint-gobain.com

E-mail: remi.lazzari@insp.jussieu.fr

E-mail: iryna.gozhyk@saint-gobain.com

**Abstract.** By combining the well-known grid reflection method with a digital image correlation algorithm and a geometrical optics model, a new method is proposed for measuring the change of curvature of a smooth reflecting substrate, a common reporter of stress state of deposited layers. This tool, called Pattern Reflection for Mapping of Curvature (PReMC), can be easily implemented for the analysis of the residual stress during deposition processes and is sufficiently accurate to follow the compressive-tensile-compressive stress transition during the sputtering growth of a Ag film on a Si substrate. Unprecedented resolution below  $10^{-5} \text{ m}^{-1}$  can be reached when measuring a homogeneous curvature. A comparison with the conventional laser-based tool is also provided in terms of dynamical range and resolution. In addition, the method is capable of mapping local variations in the case of a non-uniform curvature as illustrated by the case of a Mo film of non-uniform film thickness under high compressive stress. PReMC offers interesting perspectives for *in situ* accurate stress monitoring in the field of thin film growth.

*Keywords* : wafer curvature, stress-thickness, growth, digital image correlation, thin film

Submitted to: *Nanotechnology*

## Contents

<b>1 Introduction</b>	<b>2</b>
<b>2 Stress measurements during film growth</b>	<b>3</b>
2.1 Current stress-morphology evolution scenario during growth . . . . .	3
2.2 <i>In situ</i> stress measurement methods . . . . .	5
2.3 The PReMC method . . . . .	6
2.3.1 Experimental setup for DIC . . . . .	7
2.3.2 Formalism of curvature measurement with PReMC . . . . .	9
2.4 Comparison with MOSS technique: resolution versus measurement range . . . . .	11
<b>3 Examples of applications</b>	<b>13</b>
3.1 Growth parameters . . . . .	13
3.2 Setup description and calibration . . . . .	14
3.3 High resolution curvature measurement during Ag deposition . . . . .	14
3.4 Inhomogeneous curvature induced by a Mo film under compressive stress with a gradient of thickness . . . . .	15
<b>4 Conclusion</b>	<b>17</b>

**1. Introduction**

Due to the surge in applications of functional coatings and devices, there is an increasing need to deal with, understand and even tailor the state of residual stresses in thin films and nano-structures [1]. A wealth of experimental techniques have been developed to characterize thin film stress (or strain) state [2, 1]: (i) mechanical measurements such as nano-indentation or substrate curvature [3, 4], (ii) x-ray diffraction with all its synchrotron-based

variants that allow direct imaging of strain field through coherent diffraction [5] down to sub-micron spatial resolution, (iii) electron diffraction [6], (iv) scanning electron imaging combined with focused ion beam to follow local relaxation induced by etching [7], (v) micro-Raman spectroscopy [2]. Beyond their inherent intrinsic advantages, drawbacks or ease of access, most of them are *ex situ* or even destructive. Of all these methods, only mechanical sensors and measurements relying on surface curvature are easily implementable for *in situ* real time monitoring during deposition. In particular, substrate curvature turned out to be the technique of choice for accurate monitoring of stress build-up during the growth process of both polycrystalline and amorphous films. Its contact-less detection is compatible with the most stringent growth environments, from evaporation to sputtering, chemical vapour deposition and even electro-deposition. Its real-time monitoring capability is already used not only at the industrial scale, but also for basic understanding of growth phenomena (see reviews and references therein [8, 9, 10, 11, 12, 3, 1]) or even to engineer films with specific internal stress states and properties [13].

The technique of stress measurement through substrate curvature relies on the celebrated Stoney's law [14, 15, 3], which links the change of curvature  $\kappa$  induced in a substrate of thickness  $h_s$  upon deposition of a thin film of thickness  $h_f$  to the average stress  $\bar{\sigma}$  in the deposited layer, under the assumptions of elastically isotropic and relatively thick substrate ( $h_s \gg h_f$ ) and small induced deformations [16]:

$$\bar{\sigma}h_f = \frac{E_s h_s^2}{6(1 - \nu_s)} \kappa. \quad (1)$$

$E_s$  and  $\nu_s$  stand respectively for the Young

modulus and the Poisson ratio of the substrate. The *in situ* stress and real-time monitoring in a vacuum chamber is technically more challenging when focusing on small film thickness inducing very small curvatures and thus requiring outstanding sensitivities. In this context, this work shows how to improve both the resolution and the dynamic range of the wafer curvature technique through a full-field curvature measurement based on digital image correlation (DIC) [17, 18] analysis of a reflected pattern. The whole pattern image is analysed at different times and compared with a reference image taken before the growth. This approach, called hereafter PReMC for Pattern Reflection Mapping of Curvature, combines the above described advantages to the determination of the in-plane curvature variations across the surface, thus enabling to restore the exact shape of the deformed surface.

After an introduction on the scenario of stress evolution during metallic film growth and the requirements to accurately measure it (Section 2.1-2.2), the herein proposed PReMC method is presented in details in Section 2.3. Section 2.4 is devoted to a comparison between the resolution and measurement range obtained with the conventional multi-beam optical stress sensor (MOSS) and with PReMC setup, assuming identical measurement configurations. Finally the advantages of PReMC are illustrated by its successful applications to the following two challenging experiments: (i) the determination of rather small curvature variations during the first stages of sputter-deposition of a Ag film, where high resolution and dynamic range are necessary, and (ii) the curvature mapping of an Mo film **of non-uniform film thickness**, where sufficient resolution to in-plane curvature variations is required.

## 2. Stress measurements during film growth

### 2.1. Current stress-morphology evolution scenario during growth

In the field of thin film growth, the evolution of average stress ( $\bar{\sigma}$ ) during and after the deposition process is an indirect indicator of the complex phenomena related to the evolution of the film micro-structure during the different steps of growth (such as nucleation, grain growth, coalescence, film percolation, steady-state growth, and final relaxation). A general scenario of the interplay between stress and morphology has emerged for metals since the eighties [8, 9, 10, 11, 12, 3, 1] thanks to the development of *in situ* real time curvature measurements during vapour deposition.

Due to their micro-structure, polycrystalline films might exhibit tensile ( $\bar{\sigma}, \kappa > 0$ ) or compressive ( $\bar{\sigma}, \kappa < 0$ ) stress/strain states at different stages of the growth process, as depicted in Figure 1. **In metals deposited in conditions involving non-energetic particles, like evaporation or electrodeposition**, upon increasing the thickness, the stress-thickness  $\bar{\sigma}h_f$  of metallic films exhibits (i) a tensile stress (type I; Figure 1, green line), or (ii) a compressive-tensile-compressive stress (type II; Figure 1, blue line) behaviour [8, 9, 10, 11, 12, 3, 1]. This latter is typical of materials with low melting point  $T_m$  and high atomic mobility, characterized in most cases by a homologous temperature  $f \equiv T_s/T_m > 0.2$ , where  $T_s$  is the substrate temperature during growth [19, 8, 20]. For instance, in the case of room-temperature deposition, evaporated films of Al ( $f = 0.32$ ), Ag ( $f = 0.24$ ), Au ( $f = 0.22$ ), Cu ( $f = 0.22$ ) and Pd ( $f = 0.16$ , an exception to the em-

piric  $f > 0.2$  rule) usually exhibit a type II stress-thickness behaviour. On the opposite, evaporated films of Ta and W ( $f = 0.09$ ), Mo ( $f = 0.1$ ), Cr ( $f = 0.14$ ), Ti ( $f = 0.15$ ) and Fe ( $f = 0.17$ ) undergo a monotonous rise in tension (type I behaviour) since the beginning of the growth.

The compressive phase of type II materials at the very beginning of deposition is associated with a Volmer-Weber 3D growth [21]. Its origin is found in the surface stress and the resulting Laplace pressure experienced by each isolated island, together with a good adhesion at the interface with the substrate [22, 3]. Indeed, measurements performed on silver islands on single-crystal oxide substrates [23] have shown a change of lattice parameter mainly driven by the surface stress and eventually overwhelming the epitaxial stress induced by the crystalline substrate, above a certain island size threshold. However shortly after the beginning of the growth, the system reaches a minimum compressive stress-thickness value  $\bar{\sigma}_{co}h_{f,co}$  related to a balance of this "Laplace pressure" effect and of the tensile stress due to island coalescence and the formation of grain boundaries [24, 11, 25]. The typical reported values for Ag [26, 27, 19, 28], Au [26, 27, 19], Cu [27, 28, 29, 19], Pd [26] and Al [19] are in the range  $-0.5 < \bar{\sigma}_{co}h_{f,co} < 0$  N.m<sup>-1</sup>. Note that these values are obtained from poorly resolved dips in experimental stress-thickness curves. After this maximum, the instantaneous tensile stress due to the zipping effect of grain boundaries becomes the dominant mechanism and leads to increasing tensile stress values up to the formation of a continuous film. Finally, in type II metals, at sufficiently large film thickness, the film enters a new compressive phase. The reached maximum  $\bar{\sigma}_t h_{f,t}$  does not exceed 10 N.m<sup>-1</sup> (1.5/2.0 N.m<sup>-1</sup> for Ag [26, 27, 19, 28], 1.0/2.0 N.m<sup>-1</sup> for Au [26,

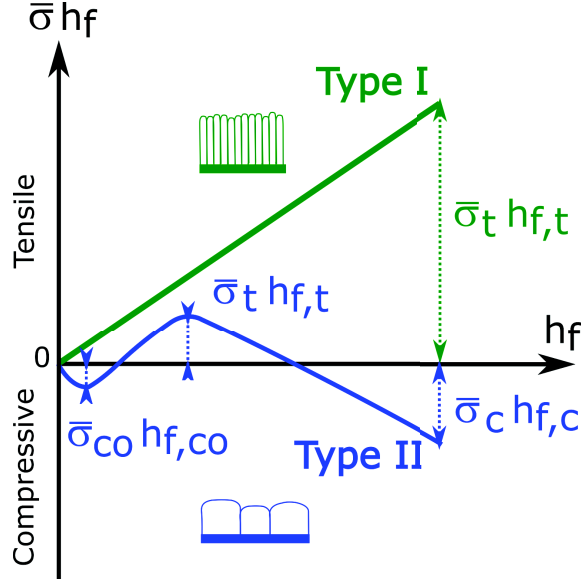


**Figure 1.** Schematic description of the stress-thickness  $\bar{\sigma}h_f$  evolution with film thickness  $h_f$  for type I (green curve) and type II (blue curve) materials. Typical grain microstructure for each type of materials is shown in insets. The physical meaning of the labels is discussed in the text.

27, 19], 2 N.m<sup>-1</sup> for Al [19], 2/4 N.m<sup>-1</sup> for Cu [27, 28, 29, 19] and 4.4 N.m<sup>-1</sup> for Pd [26]) for room-temperature growth. Although the origin of the final compressive phase remains controversial [11, 30, 21, 31, 32, 33, 34], most experiments point at a decisive role of grain boundaries [3, 35]. According to the kinetic model of Chason [30, 36, 37], a gradient of chemical potential between the surface and the interior of grain boundaries sets up due to supersaturation. This gradient drives a diffusion of adatoms into the grain boundaries inducing a compressive stress. The minimum value  $\bar{\sigma}_c h_{f,c}$  reached during this second compressive phase depends on the film thickness and for 100 nm films is in the range of  $-20 < \bar{\sigma}_c h_{f,c} < -1$  N.m<sup>-1</sup> ( $-2/ -1.5$  N.m<sup>-1</sup> for Ag [27, 19],  $-18/ -12$  N.m<sup>-1</sup> for Au [27, 19],  $-10/ -3.5$  for Cu [29, 27, 19] and  $-9$  N.m<sup>-1</sup> for Pd [26]).

Due to their low mobility, type I materials exhibit mainly a columnar growth that gives rise immediately to a strong grain boundary induced tensile stress [8, 9, 10, 11, 12, 3, 1]. Since the lateral grain size does not evolve significantly with film thickness, the stress-thickness increases roughly proportionally to the film thickness. In this case, the maximum  $\bar{\sigma}_t h_{f,t}$  is merely an indication of the maximum deposited thickness, and for 100 nm films typical values are in the range of  $60 < \bar{\sigma}_t h_{f,t} < 140 \text{ N.m}^{-1}$  (60  $\text{N.m}^{-1}$  for Ti, 120  $\text{N.m}^{-1}$  for Fe and 140  $\text{N.m}^{-1}$  for Cr [10]).

It is known that the nature of the substrate and the evaporation conditions impact significantly the previously introduced key-points ( $\bar{\sigma}_c h_{f,c}$ ,  $\bar{\sigma}_t h_{f,t}$  and  $\bar{\sigma}_{co} h_{f,co}$ ) of the stress-thickness curve (Figure 1). For instance, the deposition rate [3, 20] and the substrate temperature [27, 19] can trigger a change between type I and II behaviour. In the case of magnetron sputtering, the large kinetic energy of the incoming species acts on the evolution of the film stress state through peening and implantation mechanisms [38]; on this basis, at least two more intermediate types of film micro-structure have been reported [8, 39]. When deposited at low pressure, some type I materials such as Mo can exhibit a strong compressive state due to bombardment with energetic ions [40].

In summary, the study of the impact of deposition parameters on different stages of thin film growth may require different measurement range and resolution depending on the type of growth the material exhibits in given deposition conditions. For instance, rather large measurement range of stress thickness from 0 to up to 100-200  $\text{N.m}^{-1}$  is required for materials exhibiting type I

behaviour, while measurement range of (-20;10)  $\text{N.m}^{-1}$  with resolution of the order of 0.01 – 0.1  $\text{N.m}^{-1}$  are necessary in materials with type II behaviour.

## 2.2. *In situ stress measurement methods*

In thin film stress monitoring devices [41, 42], like in pressure and mechanical sensors that are often based on the bending of a flexible cantilever or a thin plate [43], the change of curvature of a wafer is used as to gauge the variation of exerted stress. The deflection can be measured by capacitance variation [44, 21] or piezoresistive sensors [45], but the most commonly used principle behind the contact-less detection of displacement or bending is the deflection of an optical beam [41, 42]. The well-known example is atomic force microscopy, where the deflection of a laser beam onto a cantilever is directed towards a position-sensitive detector and used to measure the tip-surface force while scanning the sample surface. To overcome mechanical drift in single beam or scanning methods [46, 9] and to improve the sensitivity, it is better to measure the relative displacements of several beams [41, 42, 47]. This principle is at the heart of the MOSS sensor [47, 3], the (commercially available [48]) reference technique for *in situ* average curvature measurement of a wafer during film growth. In this technique, a set of parallel beams is reflected by the sample and the changes in the distance between reflected beams are used to calculate the average curvature. The maximum achievable curvature resolution of MOSS, which defines the capability of the technique to capture fine details during the early stages of growth, is in the range of  $\sim 4.10^{-5}$  to  $2.10^{-4} \text{ m}^{-1}$  depending on the specific settings [26, 47, 3, 48]. In practice, the relative displacement of non-overlapping ele-

ments (beam spots in the case of MOSS) seen by a camera with a size of  $\sim 10^3$  pixels cannot be retrieved with an accuracy higher than 0.1 pixels leading to curvature resolutions of at best  $\approx 10^{-4} \text{ m}^{-1}$ , unless the image correlation is used as done herein. Regardless of this value, the actual sensitivity to small stress-thickness can be to some extent improved by using more flexible (*i.e.* having smaller bi-axial modulus  $M_s$ ; see Table 1) or thinner substrates. This possibility, that can be directly derived from Stoney's equation, is limited by the availability of wafers with uniform surface and manageable sample handling. It is illustrated in Figure 2-a for silicon wafers of different thickness. Dividing the wafer thickness by ten allows to gain two orders of magnitude in stress-thickness sensitivity and at the limit of MOSS detection to reach values of  $0.1 \text{ N.m}^{-1}$ . Figure 2-b reports the slope of the curve of Figure 2-a for different substrate materials and thickness (as given in Table 1). It is clear that the wafer thickness is a more efficient lever than the wafer stiffness to improve the sensitivity of stress-thickness measurement. A reasonable resolution for the analysis of the first compressive phase of type II materials should be of at least  $\bar{\sigma}_{co} h_{f,co}/10$ . In the case of a silver film deposited on silicon, this sets a minimum necessary curvature resolution of  $10^{-6} \text{ m}^{-1}$  in case of  $h_s = 1 \text{ mm}$  and  $10^{-4} \text{ m}^{-1}$  for  $h_s = 0.1 \text{ mm}$  silicon wafer. The first case is out-of-reach for the MOSS technique, while the second case is barely above the threshold. At the same time, a high dynamic range of at least 3 orders of magnitude is necessary to follow the different stages of growth up to 100 nm for a type II material on substrates with various stiffness values, as shown by the top blue bar in Figure 2-a.

The next sections will provide a detailed description of PReMC method and explain

how this technique can overcome the limitations of the MOSS technique.

### 2.3. The PReMC method

All PReMC predecessor methods are based on the analysis of the modified image formed by an imperfect optical element (mirror or lens). The first ancestor of the PReMC was the grating interferometer first proposed by Ronchi [56] about one century ago to obtain the curvature of (slightly) concave axisymmetric spherical mirrors. The method was further refined for the measurement of curvature variations on spherical lenses [57]. By smart positioning of the grating, of the light source and of the screen (or nowadays CCD camera detector), small curvature variations across the sample could be clearly visualized by specific fringe patterns caused by the combination of the shadow of the material grating with its image. A similar principle is employed in other techniques such as coherent gradient sensing [58, 59] (interference of the deflected beams through a system of gratings) or the grid reflection technique (deflection of a periodic grid-like image by a curved substrate [60, 61]). The maximum achievable curvature resolution with these methods can be rather high and is related to different physical factors, such as the grid or grating pitch, the sample-camera distance, the detector spatial resolution, but also the accuracy at which the features are extracted from the image of the reflected pattern.

This section will start with the description of the experimental setup used in this work for the digital image correlation (DIC, Section 2.3.1). The theoretical aspects showing how the sample curvature is deduced via a geometrical optics model from the

Material	$E_s$ [GPa]	$\nu_s$	$M_s$ [GPa]	Thickness [mm]
Si [111]	165.9 [49]	0.217 [49]	212	1.0
Si [100]*	-	-	181 [49]	0.1, 0.27, 0.5
Mica	178 [50]	0.25 [50]	237	0.05, 0.15, 0.26
Al <sub>2</sub> O <sub>3</sub>	360 [51, 52]	0.25 [52]	480	0.5
MgF <sub>2</sub>	138 [53]	0.276	191	1.0
MgO [001]	249 [54]	0.239	327	0.5, 1.0
SiO <sub>2</sub>	71.5 [55]	0.16	86.7	0.5, 1.0

**Table 1.** Elastic properties of typical substrates used in stress measurements during thin film growth: Young modulus  $E_s$ , Poisson ratio  $\nu_s$ , and bi-axial modulus  $M_s$  calculated from  $M_s = \frac{E_s}{1-\nu_s}$  except for Si[100] (non bi-axial system, see reference [49] for details).

measurement of displacements in DIC is discussed in Section 2.3.2.

*2.3.1. Experimental setup for DIC* During the curvature measurement in PReMC, the substrate surface acts as a mirror (Figure 3-a) for an illuminated pattern (Figure 4) placed outside the deposition chamber. A low-noise CCD digital camera in front of a symmetrical view-port is used to collect the reflected image which is distorted due to the variation of curvature, as shown by Figure 4. Pixel displacement maps are retrieved for each image via the simplified DIC algorithm described in reference [17] that allows for sub-pixel accuracy. A square zone of interest (ZOI) of  $\ell \times \ell$  pixels is defined around each pixel of the reflected image and a point with similar ZOI is searched in the original image recorded before the start of bending (see Figure 4). The displacement is then obtained via the coordinates of the point of maximum correlation between ZOIs. This approach is based on the assumption that the surroundings of the pixel within each ZOI do not vary much so that each ZOI can be easily recognized and retrieved. The ZOI size can be adjusted to reach a compromise between retrieval reliability, displacement map resolu-

tion, and computational time. Each image is normalized with respect to grey scale, in order to compensate for global changes in reflectance. Once the displacement of the central point is determined, the slopes, referred hereafter as zoom factors  $Z_x, Z_y$  along the  $x$  and  $y$ -axis (respectively, perpendicular and parallel to the incident plane; see Figure 3), are calculated through a linear fit of the relative displacements with respect to the initial point coordinates along the  $x$  and  $y$ -axis (see Figure 4). Based on the image formation on the camera through a lens, this approach is valid only for small zoom variation.

A typical image of the pattern used in this study recorded by the detection camera is reported in Figure 4. The original pattern is a black and white random pixel pattern ( $860 \times 860$  pixels) printed on ordinary paper ( $100 \times 100$  mm). The algorithm for pattern generation is detailed Section S1 of Supplementary Materials, and was developed to provide features of random shapes and positions with a balanced amount of black and white pixels. Provided that the features of the pattern are large enough to be resolved by the camera (several pixels [18], 15 pixels in aver-

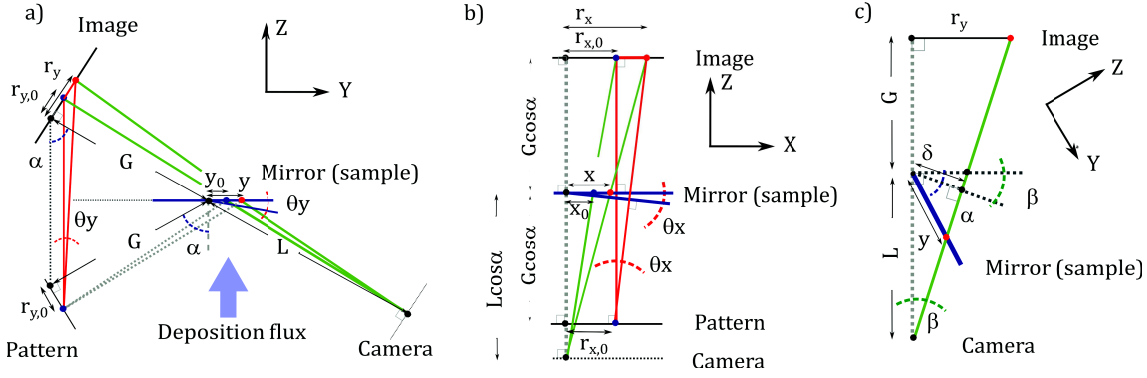


**Figure 3.** Scheme of the pattern reflection on the mirror sample surface along: (a,c) the plane of incidence (or YZ plane) and (b) the orthogonal one (or XZ plane). Distances are not on scale to improve readability. In (c), part of the YZ plane is seen along a different perspective.

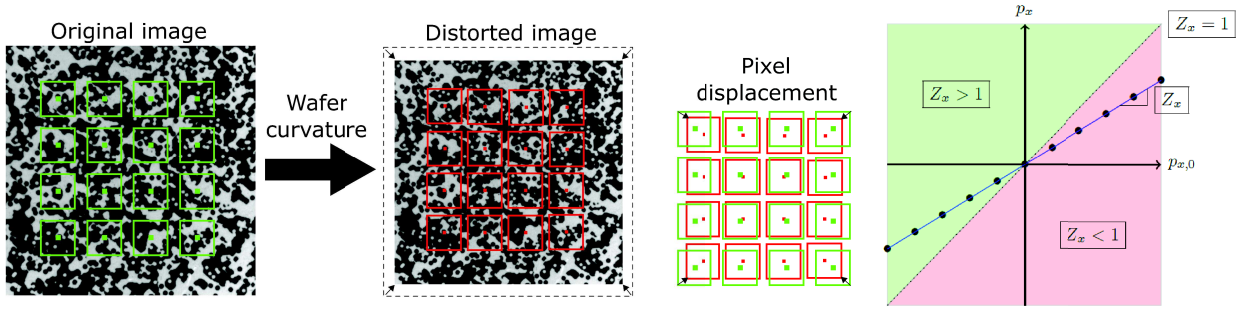


**Figure 4.** Illustration of pattern image distortion seen by the camera due to a change of sample curvature. The relative displacement of selected pixels is obtained by a DIC algorithm on their ZOIs (green/red squares). The linear regression between old and new positions gives the so-called zoom factor  $Z$ . A concave mirror ( $\kappa > 0$ ) corresponds to  $Z > 1$  and a film in tensile stress state, while for a convex mirror surface ( $\kappa < 0$ ), the stress is compressive and  $Z < 1$ . Here  $(p_{x,0}, p_{y,0})$  and  $(p_x, p_y)$  are coordinates of selected pixel before and during distortion respectively.

age for the results presented herein), they play the role of the grid pitch in the grid reflection method [60, 61] and their dimension, in a similar manner, contribute to the final resolution of the technique. The ZOI retrieval with the highest resolution is obtained if pattern image captured by the camera exhibits a smooth black to white transition between features. The final DIC displacement uncertainty depends on the ZOI dimension (see above), but also on the correlation algorithm itself. In fact, if the pattern matching is performed locally

and not on the entire image, one can improve the calculation time but one can also face accuracy problems if the displacement is out of the investigated field. In this work small displacements are assumed and this second option is used, also known as globally continuous displacement method. By doing so, a displacement uncertainty of the order of  $10^{-1}$  pixel for a ZOI of  $\ell \times \ell \approx 5 \times 5$  pixels, and even  $10^{-3}$  pixel with a ZOI of  $\ell \approx 10^2$  pixels, is achieved [18]. In the case of curvature mapping experiments, a compromise has to be found

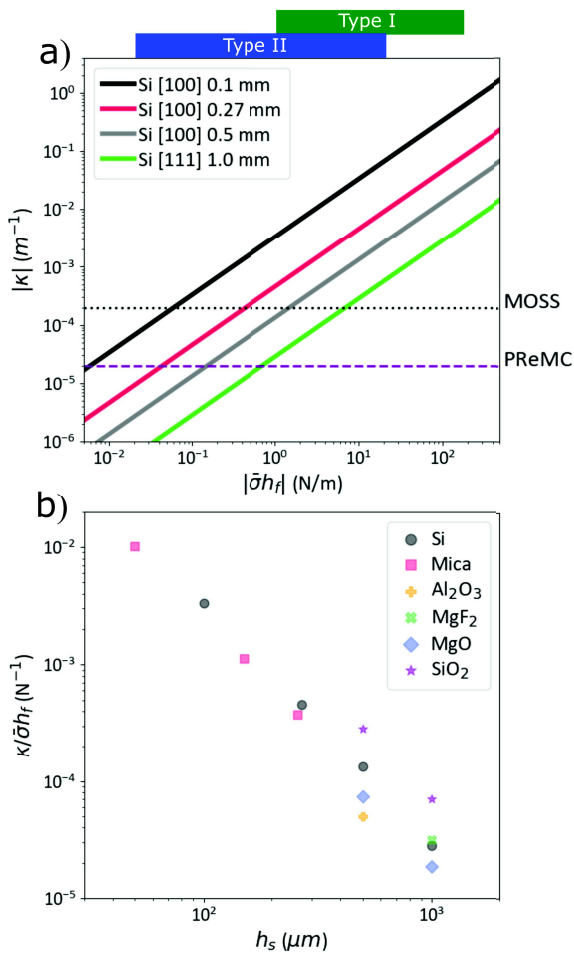


**Figure 2.** (a) Calculated curvature  $|\kappa|$ , estimated from Stoney law (Equation 1) as it would be induced on silicon wafers of different thicknesses by the deposition of a thin film exhibiting a given isotropic stress-thickness  $|\bar{\sigma}h_f|$  regardless the film material. Typical ranges of expected  $|\bar{\sigma}h_f|$  during a growth process are indicated by coloured rectangles for type I (green) and type II (blue) metals. Typical limits of resolution of MOSS and PReMC techniques are indicated by dotted lines. (b) Slope of curves such as those of Figure-a calculated for various commercially available substrates (Si, mica, MgO,  $\text{SiO}_2$ ,  $\text{Al}_2\text{O}_3$  and  $\text{MgF}_2$ ) and thicknesses, estimated from Stoney law (Equation 1) and using the elastic properties reported in Table 1.

between the absolute precision and the lateral curvature resolution. As stated above, larger ZOIs result in larger computational effort. In the case of an average curvature measurement, the uncertainty can be significantly decreased by averaging over 16 measurement points arranged in a  $4 \times 4$  square matrix, as shown in Figure 4 (known as Q4 DIC formulation). This Q4 configuration with  $\ell = 10^2$  pixels was applied herein for homogeneous films (see Section 2.3.2). With the present setup, the theoretical minimum resolvable relative displacement is of the order of  $10^{-6}$ ; nevertheless, due to noise, the actual sensitivity is estimated to be  $2 \cdot 10^{-5}$  (see Section 3).

**2.3.2. Formalism of curvature measurement with PReMC** In what follows, let's consider the general case of non-normal incidence *i.e.*  $\alpha \neq 0^\circ$ , where  $\alpha$  is the angle between the normals to the pattern and to the sample surface (Figure 3-a).  $L$  and  $G$  stand for the mirror-camera and mirror-pattern distances, respectively. If  $\alpha \neq 0^\circ$ , the reflections within the incidence plane (YZ in Figure 3-a) and within the plane normal to the incidence plane (XZ in Figure 3-b) are not equivalent; the relationships between the apparent displacement of the pattern and the local wafer slope  $\theta$  have to be analysed separately for each plane. Hereafter, the in-plane coordinates of the sample surface, of the pattern and of the camera are designated as  $(x, y)$ ,  $(r_x, r_y)$  and  $(p_x, p_y)$  respectively. The  $(y, r_y, p_y)$  coordinates correspond to the incidence plane, while  $(x, r_x, p_x)$  correspond to the plane normal to the incidence plane (see Figure 3).

Let's start with the analysis of the projection within the XZ plane (Figure 3-b). In this case the analysis is analogous

to the known case of reflection at normal incidence [61]. Note, however, that the projection of the camera-sample and sample-pattern distances in the XZ plane are reduced to  $L \cos(\alpha)$  and  $G \cos(\alpha)$ , respectively. Before deposition, the sample is assumed to be flat. The pattern element at a distance  $r_{x,0}$  from the pattern centre reflects in a point of a coordinate  $x_0$  on the sample surface. This pattern element is imaged to a point at a distance  $r_{x,0}$  from the centre of the image plane. It is seen by the camera as:

$$p_{x,0} = m \cdot r_{x,0}, \quad (2)$$

where  $m$  is the magnification of the whole optical detection system. The local change in the sample curvature results in a reflection of the same pattern point at a slightly different coordinate  $x = x_0 + \delta x$ , giving rise to an apparent shift of the image point to a distance  $r_x = r_{x,0} + \delta r_x$  from the image centre, seen as  $p_x = m \cdot r_x = p_{x,0} + \delta p_x$  by the camera. Let's call  $h(x, y)$  the distance along the z-axis from the flat mirror position for each surface point; if one considers that the axis points towards the back of the sample,  $h > 0$  ( $h < 0$ ) for samples under tensile (compressive) stress. Considering the red triangle in Figure 3-b and in the case of a small displacement [61] compared to  $L \cos(\alpha)$  and  $G \cos(\alpha)$ , the local slope along the x-direction can be calculated directly from the point displacement on the camera as:

$$\frac{\partial h}{\partial x} \equiv \tan \theta_x = \frac{\delta r_x}{2G \cos \alpha} = \frac{\delta p_x}{2mG \cos \alpha}. \quad (3)$$

The expression of the local slope along y-axis is more complex (see Section S2 of Supplementary Materials):

$$\frac{\partial h}{\partial y} \equiv \tan \theta_y = \frac{\delta p_y}{2mG} \frac{1}{1 + \frac{(2p_{0,y} + \delta p_y) \tan \alpha}{2mG}}. \quad (4)$$

This is because the point shift on the camera depends not only on the local slope, but also

on the distance of the imaged point from the pattern centre along the y-axis,  $p_y$ , and on the angle  $\alpha$ .

The general definition of local curvature reads  $\kappa \equiv d\theta/ds$ , where  $ds$  is the arc length on the curve and  $\tan \theta$  the local slope. If one considers separately the dependence along the  $x$  and  $y$  axis of the function  $h$ , it can be shown that the exact definition of curvature reads:

$$\kappa_x \equiv \frac{1}{\left(1 + \left(\frac{\partial h}{\partial x}\right)^2\right)^{\frac{3}{2}}} \frac{\partial^2 h}{\partial x^2}, \quad (5)$$

$$\kappa_y \equiv \frac{1}{\left(1 + \left(\frac{\partial h}{\partial y}\right)^2\right)^{\frac{3}{2}}} \frac{\partial^2 h}{\partial y^2}. \quad (6)$$

Most curvature measurements are based on a simplified form of these equations. In the case of small deflections, *i.e.* assuming  $ds \approx dx$  (which means that  $dh \ll dx$ ), the denominator can be neglected and the curvatures of the wafer along  $x$  and  $y$  axes,  $\kappa_x$  and  $\kappa_y$  respectively, are defined as the derivative of the local slope (out-of-plane deflections  $\tan \theta_x$  and  $\tan \theta_y$ ) along the considered direction:  $\kappa_x = \frac{\partial \tan \theta_x}{\partial x}$  and  $\kappa_y = \frac{\partial \tan \theta_y}{\partial y}$ . The second approximation used in MOSS [47, 3, 48] and grid-reflection [61] techniques is the small-angle limit  $\theta \approx \tan \theta$ . This leads to the simplified expressions  $\kappa_x = \frac{\partial \theta_x}{\partial x}$  and  $\kappa_y = \frac{\partial \theta_y}{\partial y}$ . The relative error of this approximation is smaller than  $10^{-3}$  for angles  $\theta < 3^\circ$ . For the experimental configuration used in PReMC, Equations 3 and 4 indicate that the small-angle approximation with similar relative error is satisfied if  $|\delta r_x| < 4.6$  cm and  $|\delta r_y| < 6.6$  cm. These dimensions are comparable with the half-size of the projected pattern (5 cm) and above the typical displacements observed. Nevertheless, in order to develop a method valid for other

configurations, the expressions of curvature described in this work are derived from the general exact definition of curvature (Eqs. 5 and 6). It must be said, however, that besides the approximation in the mathematical treatment due to the small angle approximation, displacements corresponding to large angles  $\theta$  would also induce image blurring due to the change of the focal plane of the image. This effect is not taken into consideration in our calculations. The exact limit angle will depend on the depth of focus of the camera lens.

Keeping in mind that the variation of the local virtual image scaling or zoom factor (see Figure 4) along the  $x$  and  $y$ -axis are  $Z_x = \frac{\partial r_x}{\partial r_{x,0}}$  and  $Z_y = \frac{\partial r_y}{\partial r_{y,0}}$  respectively, one finds (see Section S2 of Supplementary Materials for details):

$$\kappa_x = \frac{\kappa_0}{\cos \alpha} \gamma_x \left(1 - \frac{1}{Z_x}\right), \quad (7)$$

$$\kappa_y = \kappa_0 \cdot \cos \alpha \cdot \gamma_y \left(1 - \frac{\mu_y}{Z_y}\right), \quad (8)$$

$$\kappa_0 = \frac{L + G}{2LG}, \quad (9)$$

$$\gamma_x = \frac{1}{\left(1 + \left(\frac{\delta p_x}{2mG \cos \alpha}\right)^2\right)^{\frac{3}{2}}}, \quad (10)$$

$$\gamma_y = \frac{\left(1 + \frac{(p_y - \delta p_y) \tan \alpha}{mG}\right) \left(1 + \frac{p_y \tan \alpha}{m(L+G)}\right)^2}{\left(1 + \tan^2 \theta_y\right)^{\frac{3}{2}} \left(1 + \frac{2p_y - \delta p_y}{2mG} \tan \alpha\right)^2}, \quad (11)$$

$$\mu_y = 1 + \frac{\delta p_y \tan \alpha}{mG \left(1 + \frac{(p_y - \delta p_y) \tan \alpha}{mG}\right)}. \quad (12)$$

Note that  $Z \geq 1$  corresponds to tensile stress and  $Z \leq 1$  to compressive stress. In the case of a fully spherical curvature,  $\kappa_x = \kappa_y = \kappa$ . Since  $\gamma_x$  is close to unity (in the present work,  $0.997 < \gamma_x < 1$ ; see Figure S2 of Supplementary Materials), the average sample curvature can be obtained from Equation 7 through a spatial average of  $\frac{1}{Z_x}$ . Meanwhile, due to spa-

tial variations of  $\mu_y$  and  $\gamma_y$ , and their non-negligible deviations from unity (in present work,  $0.92 < \mu_y < 1.08$ ;  $0.996 < \gamma_y < 1.002$ ; see Figure S2 of Supplementary Materials), the average curvature  $\kappa_y$  should be calculated as an average over the whole curvature map from Equation 8.

#### 2.4. Comparison with MOSS technique: resolution versus measurement range

Figure 5 compares the theoretical limits of the proposed PReMC method for curvature measurement with those of the conventional MOSS technique on the basis of three parameters: (i) the maximum measurable amplitude of convex curvature due to compressive stress, (ii) the maximum measurable amplitude of the concave curvature due to tensile stress and (iii) the curvature resolution. Assuming identical measurement configurations in terms of sample-detector distance, incident angle, number of camera pixels, etc., these parameters are evaluated as a function of the initial distance between extreme imaged pattern elements  $d_0$  (laser spots for MOSS or ZOIs for PReMC; see Figure 5-d). The analysis does not account for the loss of resolution due to optical aberrations and image blurring effects, that can be observed in the case of large curvatures for both methods. In PReMC, the distance between two ZOIs will increase (decrease) under tensile (compressive) stress, while in MOSS the distance between laser spots will be subject to the opposite deformation, namely decrease (increase) under tensile (compressive) stress. Thereby, the resolution and the maximum displacement under tensile or compressive stress depend strongly on the initial distance between extreme pattern elements  $d_0$ . Due to the large tensile stress values reached during

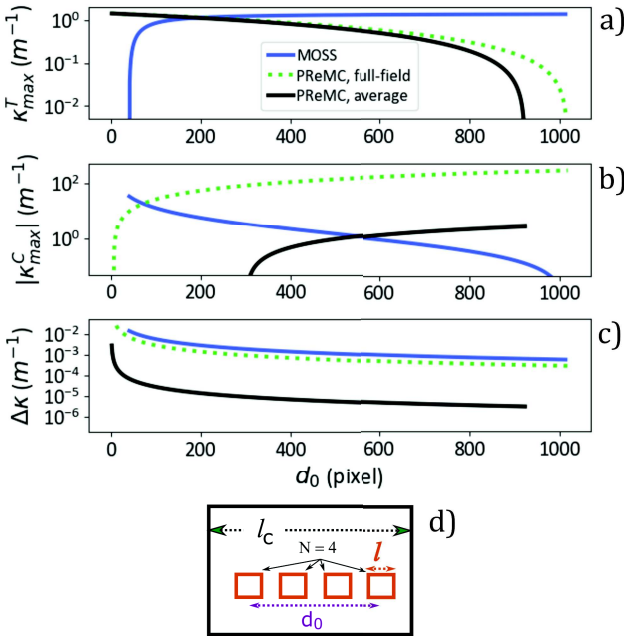


**Figure 5.** Maximum achievable measured curvature for (a) compressive  $|\kappa_{max}^C|$  and (b) tensile  $\kappa_{max}^T$  stress and (c) resolution  $\Delta\kappa$  as a function of initial distance between the extreme ZOIs  $d_0$ ; (d) schematic description of the geometrical parameters such as camera size  $l_c$ , the ZOI dimension  $l$ , the distance between extreme ZOIs  $d_0$  and the number of ZOIs  $N$ . The conventional MOSS technique is illustrated for typical configuration  $\Delta = 0.1$  pixel,  $N = 5$  and  $l = 10$  pixels. PReMC curvature measurements is illustrated by two resolution configurations: full-field with low resolution ( $l = 5$  pixels,  $\Delta = 0.1$  pixel,  $N = 4$ ; green dashed line) and averaged curvature with high resolution ( $l = 100$  pixels,  $\Delta = 0.001$  pixel,  $N = 4$ ; black line). Common  $l_c = 1024$  pixels and  $\kappa_0 = 1.41 \text{ m}^{-1}$  values are used in all depicted configurations.

growth, stress measurements on type I materials with MOSS require rather large  $d_0$  distance between pattern elements, otherwise the image points on the camera may overlap. On the other hand, stress measurements on type II materials need high sensitivity due to variations between negative and positive curvatures during different stages of the film growth (see Section 1). The optimal initial distance be-

tween pattern elements in this case depends on the explored range  $[\bar{\sigma}_c h_{f,c}; \bar{\sigma}_t h_{f,t}]$  (Figure 1). Unlike the laser spots in MOSS, note that in PReMC the ZOIs can overlap and that the initial distance between extreme ZOIs is less critical for the measurement range. It is also worth to keep in mind, that contrary to MOSS, the number of ZOIs and their dimensions in PReMC, and thereby the resolution and the measurement range, do not need to be chosen before the experiment. These parameters, and even the measurement configuration (average stress or full-field curvature analysis) can be defined at the data treatment stage.

In the MOSS method, the relative displacement of two non-overlapping elements seen by the camera can be retrieved with a resolution of  $\Delta = 0.05 - 0.1$  pixel using the moment centroiding algorithm [62]. In practice, the sensitivity is noise-limited to  $\sim 0.09$  pixel [47, 3, 48]. The number of pattern elements  $N$  (*i.e.* laser beams) is typically  $N = 5$ . The initial distance  $d_0$  can vary in the range  $[l(N-1); l_c - l]$ , where  $l_c$  is the length in pixels of the camera (typically 1024) and  $l$  that of the pattern element or spot size (typically between 5 to 100 pixels) (see Figure 5-d). In PReMC however,  $d_0$  is in the range  $[0; \frac{l_c - l}{N-1}]$  in case of averaging over several ZOIs (for example  $N = 4$  in Q4 configuration). However, in the very basic version of PReMC used for curvature mapping, only one ZOI is used to determine the evolution of the curvature at a given point and no neighbour ZOI are considered. In this case,  $d_0/2$  stands for the initial coordinate of the ZOI. Based on these parameters, Table 2 provides estimates of the extreme curvatures measurable under tensile  $\kappa_t^{max}$  and compressive  $|\kappa_c^{max}|$  strain as well as the curvature resolution  $\Delta\kappa$  for MOSS, surface-averaged and full-field modes of PReMC. All underlying

Technique	MOSS	PReMC average	PReMC full-field*
$\Delta$ (pixels)	0.05 – 0.1	0.001	0.1
$d_0$	$[\ell(N-1); \ell_c - \ell]$	$[0; \ell_c - \ell]$	$[0; \ell_c - \ell]$
$\Delta\kappa$	$\kappa_0 \frac{\Delta(N-1)}{d_0}$	$\kappa_0 \frac{2\Delta}{d_0+2\Delta}$	$\kappa_0 \frac{2\Delta}{d_0+2\Delta}$
$\kappa_{max}^T$	$\kappa_0 \frac{d_0 - \ell(N-1)}{d_0}$	$\kappa_0 \frac{\ell_c - \ell - d_0}{\ell_c - \ell}$	$\kappa_0 \frac{\ell_c - \ell - d_0}{\ell_c - \ell}$
$ \kappa_{max}^C $	$\kappa_0 \frac{\ell_c - \ell - d_0}{d_0}$	$\kappa_0 \frac{d_0 - \ell(N-1)}{\ell(N-1)}$	$\kappa_0 \frac{d_0 - \ell}{\ell}$

**Table 2.** Comparison of MOSS, surface-averaged and full-field modes of PReMC for extreme compressive  $|\kappa_c^{max}|$  and tensile  $\kappa_t^{max}$  curvatures and their respective resolution  $\Delta\kappa$ . Here  $\kappa_0 \approx \frac{1}{L \cos \alpha}$ ,  $L$  is the sample to camera distance (typically between 0.5 and 1 m) and  $\alpha$  the angle of incidence with respect to the sample normal. Expressions for PReMC were derived for  $\kappa_x$ . \*Values given in this column provide the position-dependent variation of curvature resolution and extreme values of measurable curvatures within the plane orthogonal to the incidence plane.

calculations are detailed in Section S3 of Supplementary Materials and Figure 5 depicts the corresponding variations with  $d_0$  for representative parameters.

Figure 5 shows that, for MOSS the improvement of curvature resolution comes at the expense of the reduction of the maximum measurable compressive curvature. A low-resolution mapping version of PReMC ( $\ell = 5$  pixels; green dashed line) is comparable with MOSS in terms of curvature resolution, while allowing the determination of larger compressive curvatures independently on the resolution range and larger tensile curvatures in low-resolution range. In the high-resolution version of PReMC ( $\ell = 100$  pixels; Q4; black line), the range of curvature measurements is reduced compared to the conventional technique, but a significant resolution gain of around two orders of magnitude is observed. In conclusion, with one set of measurements but via data treatment at different PReMC resolutions, it is possible to cover larger range of curvature variation and with a better resolution compared to MOSS.

### 3. Examples of applications

This section is devoted to illustrations of the capabilities of the proposed PReMC method in the case of sputtering deposition (i) to estimate the small average curvature of a Si wafer induced by a thin Ag film and (ii) to map the curvature induced by a Mo film with a thickness gradient. ZOIs of  $\ell = 100$  pixels were chosen for both cases. The section starts with a description of the used deposition conditions and of the *ex situ* calibration of PReMC setup.

#### 3.1. Growth parameters

Three types of thin films grown on a silicon substrate were studied in this work: (i) homogeneous Mo films for *ex situ* calibration of the wafer curvature technique, (ii) homogeneous Ag films to illustrate the setup resolution and (iii) inhomogeneous Mo films to exemplify the curvature mapping capability. The films were prepared by magnetron sputtering from metallic targets (of 2 inches in diameter) using pure argon (99.995%) as plasmagen gas. Before deposition, the target surface was pre-sputtered to remove surface contamination. The operating conditions for the deposition were the fol-

lowings: base pressure of  $5.10^{-5}$  Pa, substrate-target distance of 150 mm, power of 50-150 W applied to the target in direct-current mode, deposition pressure of 0.2 Pa. The deposition rates of  $0.550 \pm 0.010$  nm.s<sup>-1</sup> for Ag and  $0.115 \pm 0.002$  nm.s<sup>-1</sup> for Mo were determined *ex situ* by measuring the thickness of test samples using atomic force microscopy. The film thickness  $h_f(t)$  during growth was then deduced from deposition time and rate with a relative accuracy  $\frac{\Delta h_f}{h_f} = 1.8$  % for Ag deposition and 0.6 % for the Mo deposition. In order to grow a non-uniform film, Mo deposition was performed through a 1 cm diameter mask installed at a distance of  $\approx 70$  mm from the substrate, which is approximately half way between the sample and the magnetron target. The Mo film growths were carried out on 2 inches Si(100) wafers of  $\approx 270$   $\mu$ m thickness. In order to increase the resolution, a thinner Si(100) wafer of  $\approx 100$   $\mu$ m was employed for the stress measurements on Ag films. Substrates were used as supplied without the removal of their native oxide.

### 3.2. Setup description and calibration

The sputter-deposition chamber described elsewhere [40, 63] is equipped with two optical view-ports allowing for specular reflection on the substrate at an incidence angle of  $\alpha \approx 45^\circ$ . The pattern-sample distance  $G$  and camera-sample distance  $L$  are both of about 600 mm (Figure 3-a). The camera is placed between the sample and its mirror focal point, since the radius of curvature induced by deposition is very large. It is equipped with an objective lens with a fixed focal distance of 100 mm; the magnification of the optical detection system  $m$  is 130 pixels.cm<sup>-1</sup>. The rate of image acquisition is set at 4 frames per second, below the maximum rate of 7 frames per second.

In order to verify the geometrical parameters (which are difficult to extract accurately from a direct measurement in the vacuum chamber) and to calibrate the PReMC setup, *ex situ* measurements of curvature before and after deposition were performed on a series of reference samples made of homogeneous films of Mo on Si wafers via an optical profilometer (Chromatic Confocal Sensor Prima, STIL). The final isotropic curvature was deduced from the obtained sample height maps. Rather large values of stress-thickness can be reached with the compressive phase induced by low-pressure sputtering deposition [40]. In this work, the Mo film thickness was varied between 91 and 420 nm resulting into surface curvatures  $0.038 < |\kappa| < 0.180$  m<sup>-1</sup>. Mo was also chosen because its stress state is poorly sensitive to ageing and stable in air at ambient conditions. Moreover, PReMC measurements performed before and after venting of the deposition chamber showed constant curvature due to Mo deposition. A linear regression was performed with respect to  $\left(1 - \left\langle \frac{1}{z_x} \right\rangle\right)$  in order to verify Equation 7, yielding  $\frac{L+G}{2LG \cos \alpha} = 2.44 \pm 0.04$  m<sup>-1</sup> and  $L = G = 59$  cm, in close agreement with our previous estimations.

### 3.3. High resolution curvature measurement during Ag deposition

The stress-thickness evolution during Ag thin film deposition exhibits a type II behaviour as shown in Figure 6-a. The stress relaxation after the end of deposition is also shown in Figure 6-b. Stress-thickness is calculated at different film thickness  $0 < h_f < 40$  nm with Stoney's law (Equation 1), based on the average curvature data obtained with *in situ* measurements and substrate-related constants given in Table 1 for a wafer thickness

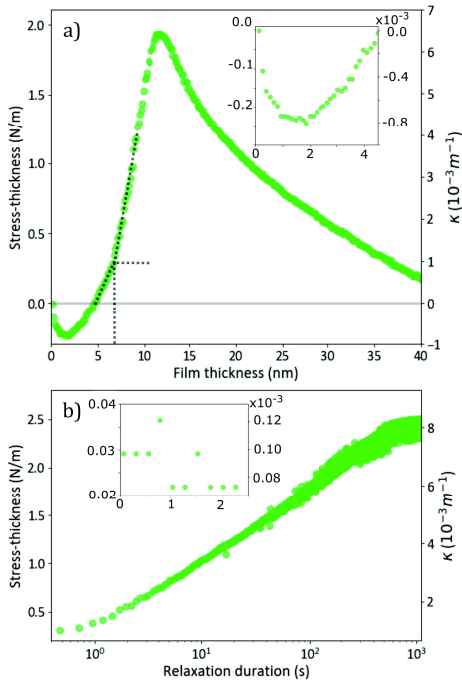


**Figure 6.** Stress-thickness (left scale) and change of wafer curvature (right scale) evolution during Ag growth on a Si substrate: (a) growth and (b) relaxation after deposition. Deposition conditions are given in Section 3.2. The inset in (a) corresponds to the zoom on the first compression phase, while the inset in (b) depicts the stress-thickness (left scale) and curvature (right scale) stabilities prior to film deposition.

of  $h_s = 100 \pm 4 \mu\text{m}$ . The relative uncertainty of film thickness is 1.8%. Thus the relative uncertainty of calculated stress-thickness value  $\frac{\Delta(\bar{\sigma}h_f)}{\bar{\sigma}h_f} = \sqrt{\left(\frac{\Delta\kappa}{\kappa}\right)^2 + \left(\frac{2\Delta h_s}{h_s}\right)^2}$  of about 8% is limited by the wafer thickness error bar  $\frac{\Delta h_s}{h_s} = 0.04$  and not really by the curvature measurement itself. Finally, the relative uncertainty of calculated stress  $\frac{\Delta(\bar{\sigma})}{\bar{\sigma}} = \sqrt{\left(\frac{\Delta(\bar{\sigma}h_f)}{\bar{\sigma}h_f}\right)^2 + \left(\frac{\Delta h_f}{h_f}\right)^2}$  is of about 8.1%.

The first compressive stage related to nucleation and growth of isolated islands is well resolved in Figure 6-a (see the inset); the min-

imum of stress-thickness associated to the beginning of their coalescence can be precisely determined ( $h_{f,co} = 1.5 \pm 0.1 \text{ nm}$  and  $\bar{\sigma}_{co}h_{f,co} = -0.23 \pm 0.02 \text{ N.m}^{-1}$  corresponding to a curvature value of  $\kappa = -7.7 \cdot 10^{-4} \text{ m}^{-1}$ ). Obviously, a curvature resolution of the order of  $10^{-5} \text{ m}^{-1}$  is necessary to resolve this first compressive stage (Figure 6-a). As depicted by the inset of the Figure 6-b, the noise-limited sensitivity of the present setup is about  $2 \cdot 10^{-5} \text{ m}^{-1}$ . The sensitivity of the present PReMC setup also makes it possible to pinpoint a striking and unexpected change of slope of the stress-thickness curve at about  $6.7 \pm 0.1 \text{ nm}$  from  $140 \pm 11 \text{ MPa}$  to  $320 \pm 26 \text{ MPa}$ . The maximum of tensile strain  $\bar{\sigma}_t h_{f,t} = 1.93 \pm 0.15 \text{ N.m}^{-1}$  indicates the formation of a continuous film at  $h_{f,t} = 11.8 \pm 0.2 \text{ nm}$ . These figures correspond to a higher stress state at lower thickness compared to previously reported values for Ag growth by sputtering and evaporation ( $1.5 \text{ N.m}^{-1}$  and about  $16 \text{ nm}$  in references [10, 26]). Finally, the incremental stress reaches a steady state of  $-42.7 \pm 3.5 \text{ MPa}$ , comparable to  $-55 \text{ MPa}$  reported for Ag deposited with magnetron sputtering at a deposition rate of  $0.1 \text{ nm.s}^{-1}$  [26]. Figure 6-b shows also that the stress-thickness after growth relaxes within approximately 11 minutes and reaches a limit value of  $2.4 \pm 0.2 \text{ N.m}^{-1}$ . The substantial increase of low frequency noise, absent during growth and starting from 100 s, originates from vibrations due to the pumping system.

### 3.4. Inhomogeneous curvature induced by a Mo film under compressive stress with a gradient of thickness

Deposition through a mask induces a non-negligible gradient of deposition rate ( $0.115$

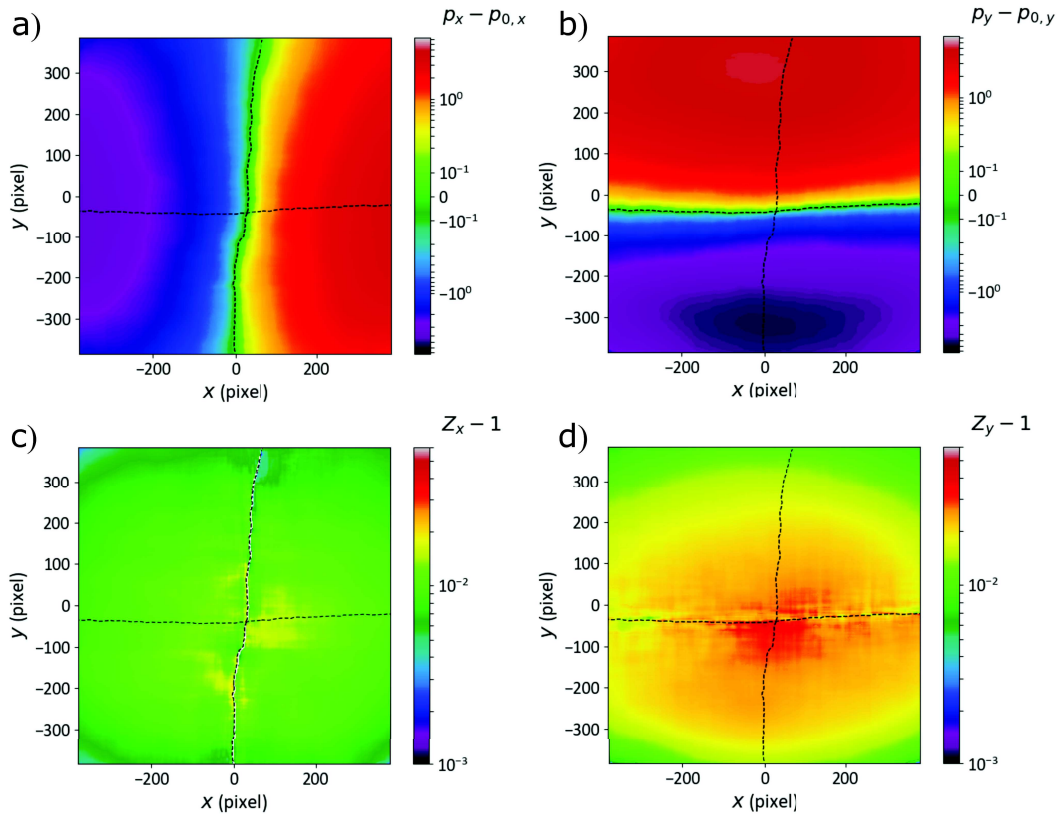


**Figure 7.** Maps of (a)(b) displacements ( $p_x - p_{0,x}; p_y - p_{0,y}$ ) and of (c)(d) zoom factors ( $Z_x - 1; Z_y - 1$ ) induced by inhomogeneous compressive curvature due to Mo deposition through a mask on a Si wafer (see text for definitions).

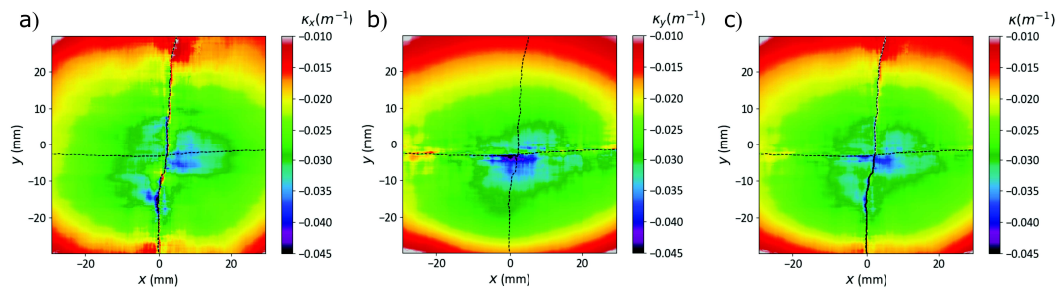


**Figure 8.** Maps of inhomogeneous curvature induced by Mo deposition through a mask: (a)  $\kappa_x$ , (b)  $\kappa_y$  and (c)  $\kappa$  (see text for definitions).

$\pm 0.002 \text{ nm.s}^{-1}$  without a mask) between the centre of the wafer and its edges, with a larger thickness in the central part and thereby a non-homogeneous distribution of surface curvature. Figures 7-a,b show the maps of the apparent displacement of the pattern along the  $x$ - and  $y$ -axis obtained at the end of deposition of a  $\sim 91 \text{ nm}$  thick film deposited through a 1-cm diameter mask. The black dash lines indicate the zero-displacement and their intersection corresponds to the centre of the sample. As expected from geometrical considerations described in Section 2.3.2, displacement along  $y$  is more prominent than along  $x$ -axis. Figures 7-c,d show the corresponding  $x$ - and  $y$ -components of zoom factors and Figure 8 the sample curvatures calculated from the displacements along  $x$ - and  $y$ -axes, and its average value. The radial symmetry of the inhomogeneous film thickness induced by the mask is clearly recovered in the total curvature (Figure 8-c). The  $x$ - and  $y$ -components are prone to artefacts due the tilt of the  $x$ - and  $y$ -axes of the camera plane with respect to the optical axis of the system.

#### 4. Conclusion

A new method for assessing the curvature of a wafer has been developed by expanding the grid reflection method with digital image correlation to reach an unprecedented resolution of below  $10^{-5} \text{ m}^{-1}$ . Apart from the accurate determination of stress in thin films and the capability to play with the compromise between accuracy and dynamic range at the data treatment stage, an other advantage of the present approach is the possibility to observe curvature variations over the sample surface to probe inhomogeneous strain fields. An example of such full-field measurement was given for a sample with a pre-designed film thickness varia-

tion; the integration of the observed displacement map can give access to the sample profile. Further improvement of the method could be achieved by optimizing the mathematical treatment of image correlation as well as the geometry of the experiment. Potential applications span from the improvement of existing mechanical sensors to accurate monitoring of stress evolution during thin film growth as illustrated herein.

#### Acknowledgments

The fruitful comments of Stéphane Roux (CNRS) on DIC method are warmly acknowledged. This work was supported by the French National Research Agency (project FRAXOS, ANR-15-CHIN-0003). Q.H. benefited from a CIFRE PhD grant funded by ANRT (Agence Nationale de la Recherche et de la Technologie) and by Saint-Gobain Recherche Paris.

#### References

- [1] G. Abadias, E. Chason, J. Keckes, M. Sebastiani, G. B. Thompson, E. Barthel, G. L. Doll, C. E. Murray, C. H. Stoessel, and L. Martinu. Review article: Stress in thin films and coatings: Current status, challenges, and prospects. *J. Vac. Sci. Technol., A*, 36(2):020801, 2018.
- [2] R. P. Vinci and J. J. Vlassak. Mechanical behavior of thin films. *Annu. Rev. Mater. Sci.*, 26:431–462, 1996.
- [3] E. Chason and P. R. Guduru. Tutorial: understanding residual stress in polycrystalline thin films through real-time measurements and physical models. *J. Appl. Phys.*, 119:191101, 2016.
- [4] C. Polop, E. Vasco, A. P. Perrino, and R. Garcia. Mapping stress in polycrystals with sub-10 nm spatial resolution. *Nanoscale*, 9:13938–13946, 2017.
- [5] I. Robinson and R. Harder. Coherent X-ray diffraction imaging of strain at the nanoscale. *Nature Materials*, 8:291–298, 2009.

- [6] A. Béch e, J. L. Rouvi ere, J. P. Barnes, and D. Cooper. Strain measurement at the nanoscale: Comparison between convergent beam electron diffraction, nano-beam electron diffraction, high resolution imaging and dark field electron holography. Ultramicroscopy, 131:10 – 23, 2013.
- [7] B. Winiarski, A. Gholinia, J. Tian, Y. Yokoyama, P. K. Liaw, and P. J. Withers. Submicron-scale depth profiling of residual stress in amorphous materials by incremental focused ion beam slotting. Acta Materialia, 60:2337 – 2349, 2012.
- [8] John A. Thornton and D.W. Hoffman. Stress-related effects in thin films. Thin Solid Films, 171:5 – 31, 1989.
- [9] W. D. Nix. Mechanical properties of thin film. Metall. Trans. A, 20:2217, 1989.
- [10] R. Koch. The intrinsic stress of polycrystalline and epitaxial thin metal films. J. Phys.: Condens. Matter, 6:9519, 1994.
- [11] F. Spaepen. Interfaces and stresses in thin films. Acta Mater., 48:31 – 42, 2000.
- [12] R. Koch. Stress in evaporated and sputtered thin films - a comparison. Surf. Coat. Technol., 204:1973 – 1982, 2010.
- [13] A. Fluri, D. Pergolesi, V. Roddatis, A. Wokaun, and T. Lippert. *In situ* stress observation in oxide films and how tensile stress influences oxygen ion conduction. Nat. Commun., 7:10692, 2016.
- [14] G. G. Stoney and C. A. Parsons. The tension of metallic films deposited by electrolysis. Proceedings of the Royal Society of London. Series A, Containing Papers of a Mathematical and Physical Character, 82:172–175, 1909.
- [15] G. C. A. M. Janssen, M. M. Abdalla, F. van Keulen, B. R. Pujada, and B. van Venrooy. Celebrating the 100<sup>th</sup> anniversary of the Stoney equation for film stress: Developments from polycrystalline steel strips to single crystal silicon wafers. Thin Solid Films, 517:1858 – 1867, 2009.
- [16] L. B. Freund, J. A. Floro, and E. Chason. Extensions of the Stoney formula for substrate curvature to configurations with thin substrates or large deformations. Appl. Phys. Lett., 74:1987–1989, 1999.
- [17] P. C. Hung and A. S. Voloshin. In plane strain measurement by digital image correlation. J. of the Braz. Soc. of Mech. Sci. & Eng., 25(3):215, 2003.
- [18] F. Hild and S. Roux. Digital image correlation: from displacement measurement to identification of elastic properties - a review. Strain, 42:69–80, 2006.
- [19] R. Abermann. Measurements of the intrinsic stress in thin metal films. Vacuum, 41:1279 – 1282, 1990.
- [20] D. Depla and B. R. Braeckman. Quantitative correlation between intrinsic stress and microstructure of thin films. Thin Solid Films, 604:90 – 93, 2016.
- [21] C. Friesen and C. V. Thompson. Reversible stress relaxation during precoalescence interruptions of Volmer-Weber thin film growth. Phys. Rev. Lett., 89:126103, Sep 2002.
- [22] R. C. Cammarata, T. M. Trimble, and D. J. Srolovitz. Surface stress model for intrinsic stresses in thin films. J. Mater. Res., 15:2468–2474, 2000.
- [23] R. Lazzari, J. Goniakowski, G. Cabailh, R. Cavallotti, N. Trcera, J. Jupille, and P. Lagarde. Surface and epitaxial stress for supported metal clusters. Nano Lett., 16:2574–2579, 2016.
- [24] W. D. Nix and B. M. Clemens. Crystallite coalescence: a mechanism for intrinsic tensile stresses in thin films. J. Mater. Res., 14:3467–3473, 1999.
- [25] S. C. Seel and C. V. Thompson. Tensile stress generation during island coalescence for variable island-substrate contact angle. J. Appl. Phys., 93:9038–9042, 2003.
- [26] G. Abadias, A. Fillon, J. J. Colin, A. Michel, and C. Jaouen. Real-time stress evolution during early growth stages of sputter-deposited metal films: Influence of adatom mobility. Vacuum, 100:36 – 40, 2014.
- [27] R. Koch, D. Winau, A. F uhrmann, and K. H. Rieder. Intrinsic stress of polycrystalline and epitaxial Ag, Cu and Au films on mica (001). Vacuum, 43:521–523, 1992.
- [28] T. Pienkos, A. Proszynski, D. Chocyk, L. Gladyszewski, and G. Gladyszewski. Stress development during evaporation of Cu and Ag on silicon. Microelectron. Eng., 70:442 – 446, 2003.
- [29] D. Winau, R. Koch, A. F uhrmann, and K. H. Rieder. Film growth studies with intrinsic stress measurement: Polycrystalline and epitaxial Ag, Cu, and Au films on mica(001). J. Appl. Phys., 70:3081–3087, 1991.
- [30] E. Chason, B. W. Sheldon, L. B. Freund, J. A.

- Floro, and S. J. Hearne. Origin of compressive residual stress in polycrystalline thin films. Phys. Rev. Lett., 88:156103, Mar 2002.
- [31] C. Friesen, S. C. Seel, and C. V. Thompson. Reversible stress changes at all stages of Volmer-Weber film growth. J. Appl. Phys., 95:1011–1020, 2004.
- [32] R. Koch, Dongzhi Hu, and A. K. Das. Compressive stress in polycrystalline Volmer-Weber films. Phys. Rev. Lett., 94:146101, Apr 2005.
- [33] J. Leib, R. Mönig, and C. V. Thompson. Direct evidence for effects of grain structure on reversible compressive deposition stresses in polycrystalline gold films. Phys. Rev. Lett., 102:256101, 2009.
- [34] H. Z. Yu and C. V. Thompson. Correlation of shape changes of grain surfaces and reversible stress evolution during interruptions of polycrystalline film growth. Appl. Phys. Lett., 104:141913, 2014.
- [35] D. Flötotto, Z. M. Wang, L. P. H. Jeurgens, and E. J. Mittemeijer. Kinetics and magnitude of the reversible stress evolution during polycrystalline film growth interruptions. J. Appl. Phys., 118:055305, 2015.
- [36] P.R. Guduru, E. Chason, and L.B. Freund. Mechanics of compressive stress evolution during thin film growth. J. Mech. Phys. Solids, 51:2127 – 2148, 2003.
- [37] A. Saedi and M. J. Rost. Thermodynamics of deposition flux-dependent intrinsic film stress. Nat. Commun., 7:10733, 2016.
- [38] H. Windischmann. An intrinsic stress scaling law for polycrystalline thin films prepared by ion beam sputtering. J. Appl. Phys., 62:1800–1807, 1987.
- [39] A. Anders. A structure zone diagram including plasma-based deposition and ion etching. Thin Solid Films, 518:4087–4090, 2010.
- [40] J. Y. Faou, E. Barthel, and S. Y. Grachev. Stress tuning in sputter-deposited MoO<sub>x</sub> films. Thin Solid Films, 527:222 – 226, 2013.
- [41] A. J. Schell-Sorokin and R. M. Tromp. Mechanical stresses in (sub)monolayer epitaxial films. Phys. Rev. Lett., 64:1039–1042, 1990.
- [42] G. J. Leusink, T. G. M. Oosterlaken, G. C. A. M. Janssen, and S. Radelaar. In situ sensitive measurement of stress in thin films. Rev. Sci. Instrum., 63:3143–3146, 1992.
- [43] J. Fraden. Handbook of modern sensors: Physics, Designs, and Applications. Springer, 2010.
- [44] R. Koch, H. Leonhard, G. Thurner, and R. Abermann. A UHV-compatible thin-film stress-measuring apparatus based on the cantilever beam principle. Rev. Sci. Instrum., 61:3859–3862, 1990.
- [45] S. C. Seel and C. V. Thompson. Piezoresistive microcantilevers for *in situ* stress measurements during thin film deposition. Rev. Sci. Instrum., 76(7):075103, 2005.
- [46] P. A. Flinn, D. S. Gardner, and W. D. Nix. Measurement and interpretation of stress in aluminum-based metallization as a function of thermal history. IEEE Trans. Electron Devices, 34:689–699, 1987.
- [47] E. Chason and J. A. Floro. Measurements of stress evolution during thin film deposition. MRS Proceedings, 436:417, 1996.
- [48] <https://www.k-space.com/products/mos/>.
- [49] G. C. A. M. Janssen. Stress and strain in polycrystalline thin films. Thin Solid Films, 515:6654 – 6664, 2007.
- [50] L. E. McNeil and M. Grimsditch. Elastic moduli of muscovite mica. J. Phys.: Condens. Matter, 5:1681–1690, 1993.
- [51] F. P. Knudsen. Effect of porosity on young’s modulus of alumina. J. Am. Ceram. Soc., 45(2):94–95, 1962.
- [52] R. M. Spriggs and L. A. Brissette. Expressions for shear modulus and Poisson’s ratio of porous refractory oxides. J. Am. Ceram. Soc., 45:198–199, 1962.
- [53] H. M. Kandil, J. D. Greiner, A. C. Ayers, and J. F. Smith. Single-crystal elastic constants of MgF<sub>2</sub> in the temperature range 4.2–300K. J. Appl. Phys., 52:759–763, 1981.
- [54] S. Adachi. Handbook on Physical Properties of Semiconductors, Volume 3 II-VI compound semiconductors, volume 3. Kluwer Academic publishers, 2004.
- [55] F. Dahmani, J. C. Lambropoulos, A. W. Schmid, S. J. Burns, and C. Pratt. Nanoindentation technique for measuring residual stress field around a laser-induced crack in fused silica. J. Mater. Sci., 33:4677–4685, 1998.
- [56] V. Ronchi. La frange di combinazione nello studio delle superfici e dei sistemi ottici. Ottica Mecca Precis, 2:9, 1923.
- [57] V. Ronchi. Forty years of history of a grating interferometer. Appl. Opt., 3:437–451, 1964.
- [58] A. J. Rosakis, R. P. Singh, Y. Tsuji, E. Kolawa, and N. R. Moore. Full field measurements

- of curvature using coherent gradient sensing: application to thin film characterization. Thin Solid Films, 325:42–54, 1998.
- [59] H. Lee, A. J. Rosakis, and L. B. Freund. Full-field optical measurement of curvatures in ultra-thin-film-substrate systems in the range of geometrically nonlinear deformations. J. Appl. Phys., 89:6116–6129, 2001.
- [60] V. J. Parks. Surface curvature analyzed with a grid-reflection technique. Exp. Mech., 24:44–47, 1984.
- [61] M. Finot, I. A. Blech, S. Suresh, and H. Fujimoto. Large deformation and geometric instability of substrates with thin-film deposits. J. Appl. Phys., 81(8):3457–3464, 1997.
- [62] T. Schildknecht. Optical Astrometry of Fast Moving Objects Using CCD Detectors. Geodätisch-geophysikalische Arbeiten in der Schweiz. Institut für Geodäsie und Photogrammetrie, 1994.
- [63] I. Gozhyk, L. Dai, Q. Hérault, R. Lazzari, and S. Grachev. Plasma emission correction in reflectivity spectroscopy during sputtering deposition. J. Phys. D: Appl. Phys., 52:095202, 2018.